JOURNAL OF PROPULSION AND POWER
Vol. 24, No. 5, September–October 2008

Single-Dielectric Barrier Discharge Plasma Enhanced Aerodynamics: Concepts, Optimization, and Applications

Thomas C. Corke*
University of Notre Dame, Notre Dame, Indiana 46556
and
Martiqua L. Post† and Dmitriy M. Orlov‡
U.S. Air Force Academy, Colorado Springs, Colorado 80840

DOI: 10.2514/1.24430

This paper deals with the physics and design of single dielectric barrier discharge plasma actuators for enhanced aerodynamics in a variety of applications. The actuators consist of two electrodes: one exposed to the air and the other covered by a dielectric material. The electrodes are supplied with an alternating current voltage that, at high enough levels, causes the air over the covered electrode to ionize. The ionized air, in the presence of the electric field produced by the electrode geometry, results in a body force vector that acts on the ambient air. The body force is the mechanism for active aerodynamic control. The plasma generation is a dynamic process within the alternating current cycle. The body force per unit volume of plasma has been derived from first principles and implemented in numerical flow simulations. Models for the time and space dependence of the body force on the input voltage amplitude, frequency, electrode geometry, and dielectric properties have been developed and used along with experiments to optimize actuator performance. This paper presents results that highlight the plasma actuator characteristics and modeling approach. This is followed by overviews of some of the applications that include leading-edge separation control on airfoils, dynamic-stall vortex control on oscillating airfoils, and trailing-edge separation control on simulated turbine blades.

Nomenclature

C	=	capacitance
C_D	=	drag coefficient
C_L	=	lift coefficient
c	=	wing chord
D	=	drag force
f	=	excitation frequency of unsteady plasma actuator
f_b	=	body force
I	=	current
L	=	lift force
L_{sep}	=	streamwise extent of separation zone
P	=	power
q	=	dynamic pressure
R	=	resistance
Re_c	=	Reynolds number based on chord length and freestream velocity
St	=	Strouhal number $= fc/U_\infty$
t	=	time
U	=	mean streamwise velocity
U_∞	=	freestream velocity
u'	=	root mean square of streamwise velocity fluctuations
V	=	plasma actuator voltage
x, y	=	axial coordinates
α	=	angle of attack
α_{0L}	=	zero lift angle of attack

Subscripts

app	=	applied
max	=	maximum value
n	=	index
p	=	plasma
$p-p$	=	peak-to-peak level
s	=	condition at stall

I. Introduction

PLASMA-enhanced aerodynamics have been demonstrated in a range of applications involving separation control, lift enhancement, drag reduction, and flight control without moving surfaces [1–7]. The fundamental component for this are "plasma actuators." The plasma actuator consists of two electrodes that are separated by a dielectric material. One of the electrodes is exposed to the air. The other electrode is fully covered by the dielectric material. A schematic illustration of the actuator configuration used in the cited applications is shown in Fig. 1. A high voltage alternating current (ac) input is supplied to the electrodes. When the ac voltage amplitude is large enough, the air ionizes in the region of the largest electric potential. This generally begins at the edge of the electrode that is exposed to the air and spreads out over the area projected by the covered electrode. The location of the plasma is denoted in Fig. 1.

The process of ionizing the air in this configuration is classically known as a single dielectric barrier discharge (SDBD) [8]. It has the property that it is self-limiting and, therefore, stable at atmospheric pressures [8,9]. During the ac cycle, the electrons and ions move according to the sign in the alternating electric potential. As they move, the surface of the dielectric becomes charged. When the potential difference between the exposed electrode and the dielectric surface is large enough, the air over the dielectric layer ionizes. This continues until the charge on the dielectric surface builds up to the point that the potential difference is below the threshold for ionization, and the process stops. This is the self-limiting aspect of the dielectric barrier: it prevents a cascade of charges that would cause an electric arc and distinguishes it from other approaches that use an air gap between uncovered electrodes. With the SDBD

Received 4 April 2006; revision received 21 March 2008; accepted for publication 21 March 2008.

*Clark Chair Professor, Center for Flow Physics and Control, Aerospace and Mechanical Engineering Department.
†Assistant Professor of Aeronautics, Department of Aeronautics.
‡Research Fellow, Department of Physics, Space Physics and Atmospheric Research Center, 2354 Fairchild Drive.

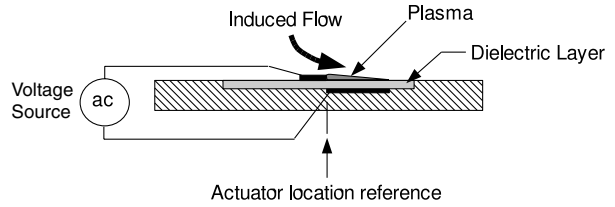

Fig. 1 Schematic drawing of SDBD plasma actuator illustrating asymmetric electrode arrangement, dielectric layer, and location of plasma formation. The actuator location is referenced to the junction of the exposed and covered electrodes.

approach, there is minimal heating of the air, and temperature change is not the mechanism for flow control.

A key element in improving the performance of the SDBD plasma actuators is understanding and modeling the dynamic process in which the air is ionized during the ac cycle. One of the first models for a dielectric barrier discharge (DBD) plasma actuator was developed by Massines et al. [10] It was a one-dimensional model based on a simultaneous solution of the continuity equations for charged and excited particles and the Poisson equation.

Paulus et al. [11] developed a particle-in-cell simulation to study the time-dependent evolution of the potential and the electrical field surrounding two-dimensional objects during a high voltage pulse. The numerical procedure was based on the solution of the Poisson equation on a grid in a domain containing an L-shaped electrode to the determine the movement of the particles through the grid. The simulation showed that the charged particles move toward the regions of high electric potential, creating a high electric field strength near the electrode's edges. In addition, it showed that the plasma builds up on a very short, microsecond, time scale.

Orlov et al. [12] studied the ionization process through space–time measurements of the plasma light emission over the actuator, which are known to correlate with the current through the actuator [8]. Their experimental setup is illustrated in Fig. 2. It consisted of a photomultiplier tube (PMT) that used a double slit to focus on a narrow 2-D region of the plasma. The long axis of the 2-D region was aligned to be parallel to the edge of the exposed electrode. The location of the viewed region was varied to reveal the spatial character of the plasma. The output of the PMT was ensemble averaged using the ac cycle as a phase reference. An example of an ensemble averaged time trace from the PMT output at an intermediate distance from the edge of the exposed electrode is shown in Fig. 3. The corresponding input voltage time series is also shown for reference.

The regions where the narrow spikes in PMT time series occur correspond to the part of the ac cycle when the air is ionized. The ionization is generally uniform except for some sparsely distributed, random microdischarges that are more intensely illuminated and, therefore, more easily sensed by the PMT. The ensemble averaging causes these random events to accumulate and fill the time interval in which the air is ionized.

We observe that the air separately ionizes twice in the ac period and that the intensity of these two events is not equal. Similar behavior was found by Enloe et al. [8], with the difference in the two

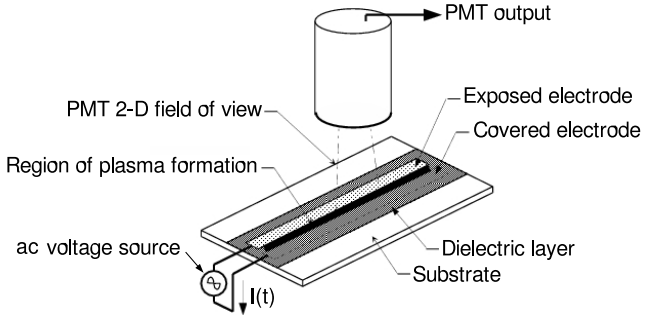

Fig. 2 Experimental setup used in measuring plasma light emission for SDBD model validation. From Orlov et al. [12].

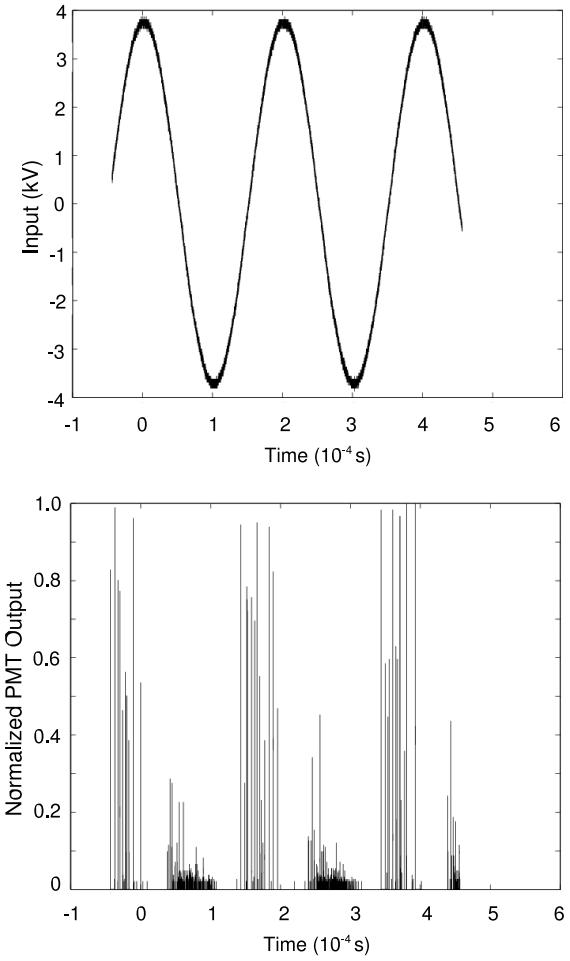

Fig. 3 Time series of input voltage (top) and PMT output proportional to the light emission in a narrow 2-D region over the dielectric layer (bottom) for SDBD plasma actuator. From Orlov et al. [12].

events associated with the difference in the ability to deposit or remove charges from the dielectric. An experiment in which both electrodes were covered by a dielectric layer (double dielectric) showed perfect symmetry of the two events [8]. This behavior suggests that a more optimum waveform to maximize the amount of ionization during the ac cycle would be a sawtooth with the long rise time corresponding to the portion when the electric potential direction is depositing electrons on the dielectric [8].

A composite of light emission time series measured at different positions over the dielectric surface is shown in Fig. 4. These are shown as contours of constant light intensity for one period of the ac cycle. The x axis is the distance over the covered electrode measured from the edge of the exposed electrode. On the time axis, $t/T = 0$ corresponds to the $t = 0$ in the input ac cycle shown in Fig. 3.

The space–time character of the plasma light emission over the covered electrode has a number of interesting features. For example, there is a sharp amplitude peak near the edge of the exposed electrode at the first initiation of the plasma. As time increases, the plasma sweeps out from the junction to cover a portion of the encapsulated electrode. As the plasma sweeps out away from the edge of the exposed electrode, its light emission becomes less intense. Our estimates are that the intensity decreases exponentially from the junction. This led to the exponential weighting we have used in estimating the spatial dependence of the body force in our direct Navier–Stokes (DNS) simulations [13–15]. Two of the global features of the space–time evolution of the plasma formation are the velocity at which the plasma front moves across the dielectric and the maximum extent of the plasma during the ac cycle. The velocity is represented by the slope $\mathrm{d}x/\mathrm{d}t$ of the front. We note that the velocity of the fronts is approximately the same for the two halves of the ac cycle, but the plasma extent differs.

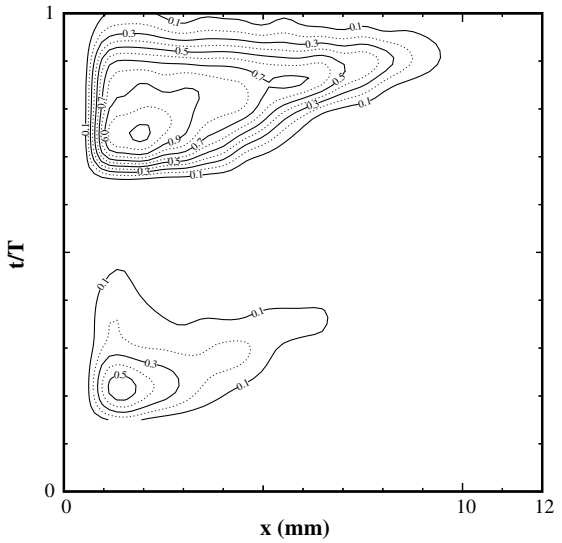

Fig. 4 Space–time variation of the measured plasma light emission for SDBD plasma actuator corresponding to one period T of the input ac cycle. From Orlov et al. [12].

II. Single Dielectric Barrier Discharge Plasma Modeling

A. Lumped-Element Model

Although it is possible in principle to compute the space-time evolution of the ionized air in the operation of the SDBD plasma actuator, the computational overhead is significant, except possibly in 1-D. As an alternative, following the temporal model of Enloe et al. [8], Orlov and Corke [14] and Orlov et al. [12] have been developing models for the space–time evolution of the plasma using lumped-circuit elements. The advantage of these models is that they provide an efficient design tool for examining the effects of such parameters as electrode geometry, dielectric material properties, ac frequency, and ambient conditions on the performance of the plasma actuators.

An example of the lumped-element model of Orlov et al. [12] is shown in Fig. 5. With this, the physical space over the dielectric-covered electrode is divided into N small subregions as shown in the top part of the figure. Each of the subregions corresponds to a parallel circuit arrangement as shown in the bottom part of the figure.

Each of the parallel subcircuits consists of an air capacitor, a dielectric capacitor, and a plasma resistive element. The zenor diodes in the subcircuits determine the voltage levels at which the plasma initiates and the different plasma resistances based on the current direction, as observed in the experiments. The air capacitor in the nth subcircuit is defined as

$$C_{an} = \frac{\varepsilon_0 \varepsilon_a A_n}{l_n} \tag{1}$$

where ε_a is the dielectric coefficient of air, l_n is the length of the air capacitor in the subcircuit n, and A_n is the cross section of this air capacitor. The resistance in the nth subcircuit is defined as

$$R_n = \frac{\rho l_n}{A_n} \tag{2}$$

where ρ is the resistivity of the air. The dielectric capacitor for each subcircuit is defined as

$$C_{dn} = \frac{\varepsilon_0 \varepsilon_d A_d}{l_d} \tag{3}$$

where ε_d is the dielectric coefficient of the dielectric material used, l_d is the thickness of this material, and the cross section A_n is defined by the total number of the subcircuits.

If the applied voltage is a given function, then the value of the voltage on the surface of the dielectric in the subcircuit n can be described by

$$\frac{\mathrm{d}V_n(t)}{\mathrm{d}t} = \frac{\mathrm{d}V_{\mathrm{app}}(t)}{\mathrm{d}t}\left(\frac{C_{an}(t)}{C_{an}(t)+C_{dn}(t)}\right) + k_n \frac{I_p(t)}{C_{an}(t)+C_{dn}(t)} \tag{4}$$

where $k_n = 0$ if the plasma is not present in the nth subcircuit, or $k_n = 1$ if the plasma is present in the nth subcircuit. $I_p(t)$ is the plasma current given by

$$I_p(t) = \frac{1}{R_n}[V_{\mathrm{app}}(t) - V_n(t)] \tag{5}$$

where $R_n = R_{nf}$ or $R_n = R_{nb}$ depends on the direction of the current in the plasma.

The plasma is the only dissipative element in the circuit. The instantaneous power $P(t)$ is then

$$P(t) = I_p(t)|V_{\mathrm{app}}(t) - V_{2A}(t)| \tag{6}$$

The electric circuit Eq. (4) for the N subcircuits is solved to obtain the voltage potential on the surface of the dielectric $V_n(t)$ and the plasma current $I_p(t)$. An example of the result is shown in Fig. 6. The figure shows contours of constant rectified current $|I_p|$ as a function

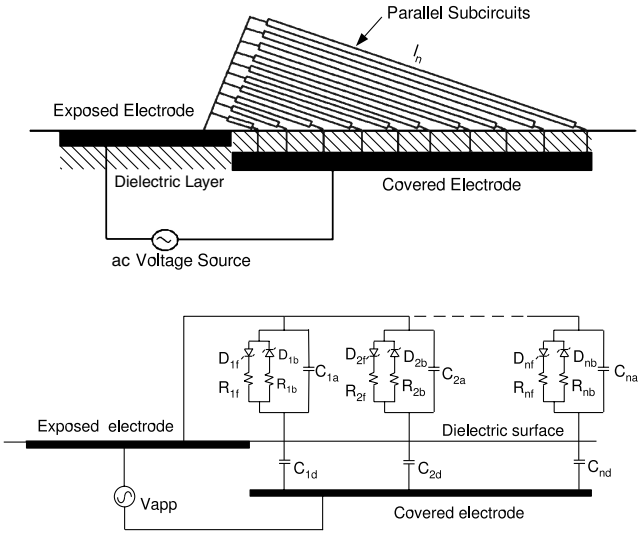

Fig. 5 Lumped-circuit model of a SDBD plasma actuator with the space over the covered electrode divided into N parallel subcircuits. From Orlov et al. [12].

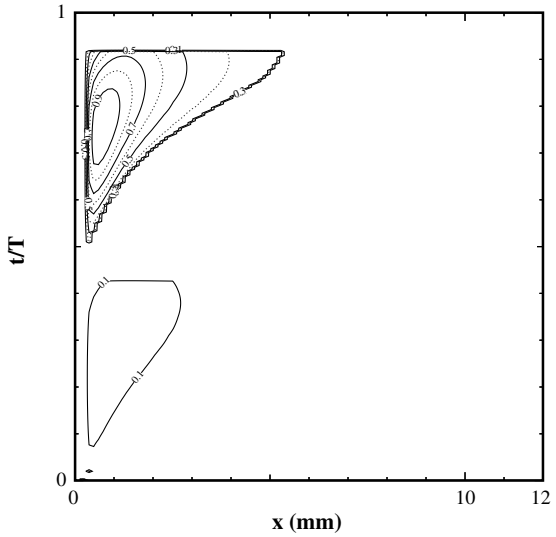

Fig. 6 Space–time variation of rectified current $|I_p|$ over dielectric-covered electrode from lumped-circuit model of SDBD plasma actuator. From Orlov [31].

of time and space during one period of the input ac cycle. As pointed out, the current has been found to correlate with the plasma illumination intensity. The presentation of the rectified current is then meant to compare to the space–time contours of plasma illumination that were shown in Fig. 4. The space–time character of the current from the lumped-circuit model has the same general character as the measured illumination. This can be further refined as estimates of some of the properties of the ionized air improved. However, as it is, it provides a first-order estimate of the space–time variation of the electric potential that will be needed to calculate the effect of the actuator on the ambient air. Comparisons of properties such as the plasma sweep velocity and maximum extent as a function of the input ac voltage amplitude from the model showed excellent agreement with experiments [12].

B. Body Force

The plasma produced by the actuator is an ionized quasi-neutral gas. In the general case, the system can be represented by the set of four Maxwell's equations. We assume that the ac period is long compared with the time needed for the charges in the plasma to redistribute themselves so that, on the whole, the system is quasi steady. In this case, the group of Maxwell's equations that describe the system of charges with charge density ρ_c, reduce to

$$\operatorname{div} \mathbf{D} = \rho_c \tag{7}$$

Here, the vector of electric induction $\mathbf{D}$ is related to the vector of electric-field strength $\mathbf{E}$ through the dielectric coefficient ε as

$$\mathbf{D} = \varepsilon \mathbf{E} \tag{8}$$

By definition, if an electric potential φ is known as a function of space coordinates, then it is possible to compute an electric-field strength $\mathbf{E}$ by

$$\mathbf{E} = -\nabla\varphi \tag{9}$$

Equation (7) then becomes

$$\nabla(\varepsilon\nabla\varphi) = -\frac{\rho_c}{\varepsilon_0} \tag{10}$$

To examine the behavior of the charges in the electric field, we consider a 1-D case with the electric field acting in direction s. The equation of the motion of the plasma gas due to the electric field is then

$$mn\left[\frac{\partial \mathbf{u}_p}{\partial t} + (\mathbf{u}_p \cdot \nabla)\mathbf{u}_p\right]_s = qnE - \frac{\partial p}{\partial s} \tag{11}$$

where m is the mass of the ion particle, n is the number of the particles in the plasma gas, u_p is the velocity of the plasma gas, q is the charge of the particle, and p is the pressure of the plasma gas. Ignoring the diffusion processes and assuming that the system is in steady state and that velocity gradients can be ignored, the left side of the Eq. (11) vanishes. Substituting for the pressure gradient ∇p (for isothermal gas we have $\nabla p = k_b T \nabla n$, where k_b is the Boltzmann's constant, T is the temperature of the plasma gas, and n is the number of the particles in the plasma gas), we obtain

$$qnE = k_b T \frac{\partial n}{\partial s} \tag{12}$$

In the plasma under consideration, the ions lose only one electron and have the charge $q = -e$, where e is the charge of the electron. Applying Eq. (9) to the 1-D electric field $E = -\frac{\partial \varphi}{\partial s}$ so that

$$e\frac{\partial \varphi}{\partial s} = \frac{k_b T}{n}\frac{\partial n}{\partial s} \tag{13}$$

The solution of Eq. (13) is the Boltzmann relation

$$n = n_0 \exp\left(\frac{e\varphi}{k_b T}\right) \tag{14}$$

where n_0 is the number of the molecules that were separated into ions and electrons by the electric field, the so-called background plasma density.

It can be seen from Eq. (14) that the charged particles have larger concentration in the regions of the high electric potential. According to this equation, their density decays exponentially. Without loss of generality, these results can be extended to the two-dimensional case.

The net charge density at any point in the plasma is defined as the difference between the net positive charge produced by ions and the net negative charge of electrons. The difference can be related to the local electric potential φ by the Boltzmann relation (14). Assuming a quasi-steady state, with a long enough time scale for the charges to redistribute themselves,

$$\rho_c = e(n_i - n_e) \approx -en_0\left(\frac{e\varphi}{kT_i} + \frac{e\varphi}{kT_e}\right) \tag{15}$$

where $T_{i,e}$ are temperatures of ions and electrons.

Substituting for the charge density Eq. (15) into the Maxwell's Eq. (10), leads to the electrostatic equation for our problem:

$$\nabla(\varepsilon\nabla\varphi) = \frac{1}{\lambda_D^2}\varphi \tag{16}$$

where λ_D is called the Debye length, which is the characteristic length for electrostatic shielding in plasma.

The Debeye shielding is valid if there are enough charged particles. A parameter that characterizes unmagnetized plasma systems is the dimensionless plasma parameter Λ defined as

$$\Lambda = \frac{4}{3}\pi\lambda_D^3 n_e \tag{17}$$

If $\Lambda \gg 1$, then it signifies that the plasma is weakly coupled, and the Debye shielding is valid. For the plasmas of consideration, the Debye length is approximately 0.00017 m, and the density of the charged particles is on the order of 10^{16} particles/m^3 [16]. In this case, $\Lambda = 3.5 \times 10^5$, and the assumption of the Debye shielding is valid.

The value of the electric potential in the SDBD arrangement is set by the potential on the exposed electrode

$$\varphi|_{\text{electrode}} = \pm\varphi_0 \tag{18}$$

and on the surface of the dielectric, which acts as a virtual electrode,

$$\varphi|_{\text{surface}} = \varphi_s(x) \tag{19}$$

For the applied ac voltage, the electric potential varies in space on the dielectric surface covering the electrode during the ac period. In the lumped-circuit model, this is denoted as $V_n(t)$. At any time instant, this is equated to $\varphi_s(x)$ in defining the boundary condition in the solution of the electrostatic Eq. (16).

The boundary conditions on the outer boundaries model the condition at the "infinity," where the electric potential φ is equal to zero

$$\varphi|_{\text{outer boundary}} = 0 \tag{20}$$

The solution of the electrostatic Eq. (16) is the electric potential φ. The electric-field strength E is related to φ through Eq. (9). If we assume a value of λ_D, ρ_c can be found as

$$\rho_c = -\frac{\varepsilon_0}{\lambda_D^2}\varphi \tag{21}$$

Because there is an electric field in the plasma in regions where there is also a net charge density, there will be a force on plasma. The electric force acting on a single charge is given by Lorentz equation:

$$\mathbf{f}_b = q\mathbf{E} \tag{22}$$

The force density, which acts on a continuous system of charges with charge density ρ_c, can be written as

$$\mathbf{f}_b = \rho_c \mathbf{E} = -\left(\frac{\varepsilon_0}{\lambda_D^2}\right)\varphi \mathbf{E} \tag{23}$$

This body force Eq. (23) is a body force per volume of plasma, which varies in time and space during the ac cycle.

The method of solution to obtain the body force starts with the lumped-element model, which determines the space-time distribution of charge on the surface of the dielectric. This sets the time-dependent boundary conditions on $\varphi_s(x)$ that are used in solving the electrostatic Eq. (16) for φ. The electric field $\mathbf{E}$ is then found from the solution of Eq. (9). The body force vector is then found from the body force Eq. (23).

This body force vector can be tailored through the design of the electrode arrangement and dielectric material, which control the spatial electric field. The body force representation is also a convenient form to incorporate the effect of the actuators in Navier–Stokes (N–S) simulations of the flowfield. Such N–S simulations have been used to design and optimize different plasma actuator arrangements [13,17,18]. Another actuator optimization comes from the choice of the ac time series shape, which controls the duration and extent of the plasma [8,9].

In flow simulations, the body force enters the governing equations for the flow in the momentum equation. This implies that the effect of multiple actuators has an additive effect on the momentum. Post [3] performed experiments to investigate this. Results of this are shown in Fig. 7. This involved measuring mean velocity profiles of the actuator-induced flow at a fixed distance from a series arrangement of SDBD plasma actuators having the asymmetric electrode design shown in Fig. 1. The asymmetric electrode design results in a body force that induces the flow in the direction from the exposed electrode toward the covered electrode (see arrow in Fig. 1). This produces a wall-normal mean velocity distribution that is similar to a tangential wall jet. The left plot in Fig. 7 documents examples of the profile shape. Each symbol corresponds to separate measured profiles. The number before the "A" in the label indicates the number of actuators being operated at one time (1, 2, or 3) in this figure. Profiles like these were integrated in the wall-normal direction to determine the momentum produced by the actuators. This has been normalized by the momentum with one actuator operating. The symbols labeled "Higher V_{app}" correspond to the profiles that were presented in the left part of the figure. The other symbols were at a lower applied voltage and investigated up to five series actuators. Because the actuator effect acts as a body force, we expect that the induced momentum would be linear with the number of actuators. The dashed line indicates that trend. It appears that the data approximate that behavior, especially when two to five actuators are operating. This summing effect of the plasma actuator supports the body force model and points to an approach for improving its effectiveness in high-speed applications.

Post [3] has shown that the peak velocity in profiles like those in Fig. 7 for a single actuator varies as $V_{app}^{7/2}$. This is documented in Fig. 8 as the open symbols. The closed symbols correspond to the dissipated power based on the lumped-circuit model described in the previous section. We note that the power has the same $V_{app}^{7/2}$ dependence as the maximum velocity. Enloe et al. [8] observed the same dependence on thrust produced by a SDBD plasma actuator.

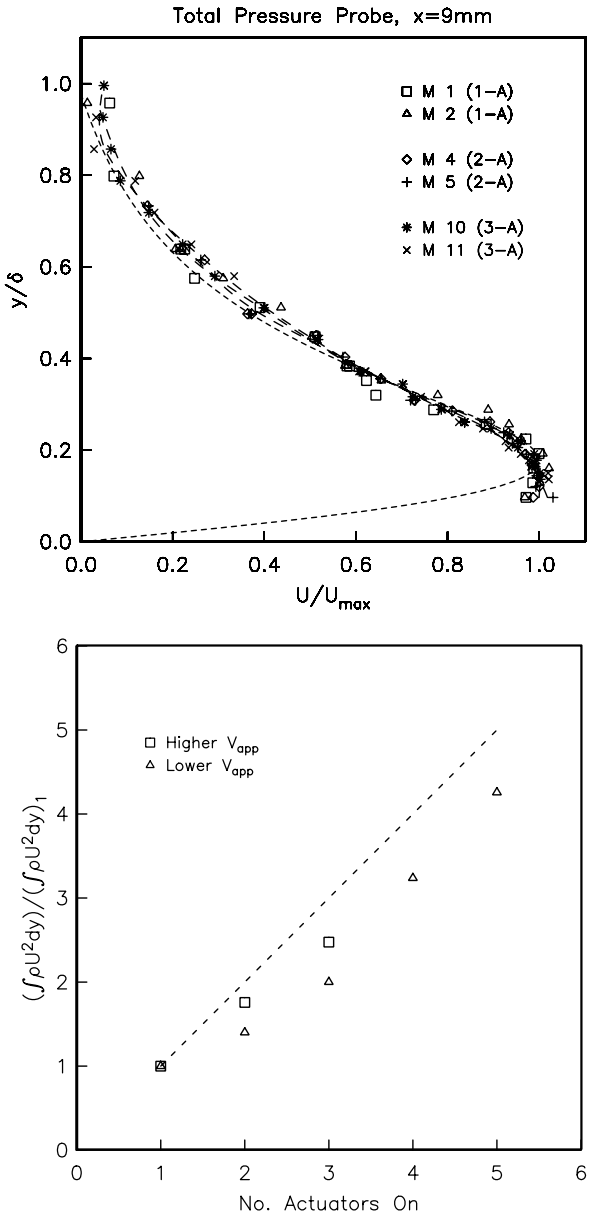

Fig. 7 Normalized mean velocity profiles (top) and normalized momentum (bottom) of the actuator-induced flow for different numbers of SDBD plasma actuators arranged in series. Measurement made 9 mm from edge of exposed electrode. From Post [3].

III. Sample Applications of SDBD Plasma Actuators

The SDBD plasma actuators have been successfully used in numerous flow control applications. These include exciting 3-D boundary layer instabilities on a sharp cone at Mach 3.5 [19], lift

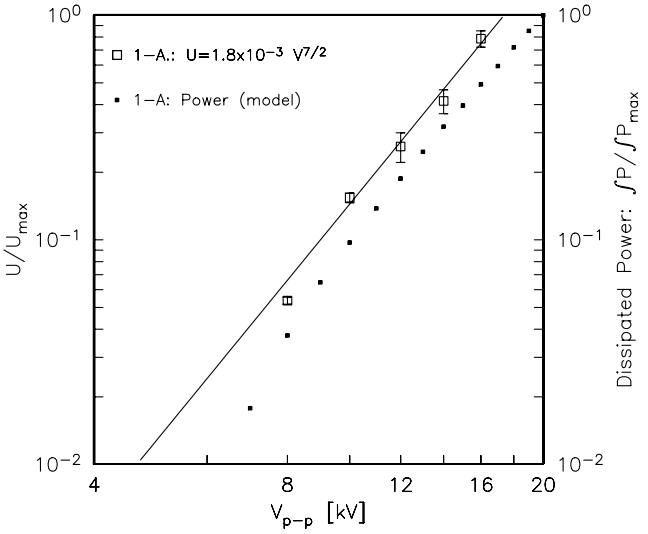

Fig. 8 Dependence of plasma actuator maximum induced velocity (open symbols) and plasma dissipated power based on lumped-circuit model (closed symbols) as a function of applied ac voltage. Power calculations from Orlov and Corke [14].

augmentation on wings [6], separation control for low-pressure turbine blades [2,20–23], leading-edge separation control on wing sections [1,5,24], boundary layer drag reduction [25], and control of the dynamic-stall vortex on oscillating airfoils [3,4].

The success in experiments has led to a number of flow simulations that incorporate some of the plasma actuator effects. These include those by Visbal and Gaitonde [24], Gaitonde et. al [26], and Suzen et al. [27,28].

This paper summarizes some of these applications to demonstrate its use and highlight its potential.

A. Leading-Edge Separation Control

The following illustrates the use of plasma actuators in the control of leading-edge separation on stationary wing sections. The approach is to locate an actuator directly on the leading edge that is designed to induce a flow toward the suction side of an airfoil at angles of attack. This has been demonstrated on a number of 2-D airfoil shapes including NACA 0009, 0012, 0021, 66_3-018, and an HS3412. The chord Reynolds numbers in these experiments ranged from 77 to 860 K and encompassed freestream speeds from 10 to 38 m/s [1,3,5]. Figure 9 illustrates this on a NACA 0015 airfoil [5]. Also included are body force vectors based on the SDBD actuator model.

The plasma actuator consists of two electrodes fabricated from 0.05-mm-thick copper foil tape. The dielectric layer is Kapton film. We use a number of different thicknesses ranging from 0.025 to 0.127 mm. The choice of the thickness is generally based on the maximum voltage we anticipate using, with the breakdown voltage of the Kapton film being approximately 6 kV per 0.025 mm thickness. The dielectric constant is 3.3.

The plasma actuator is bonded directly to the surface of the airfoil. At the leading edge, where the flow is sensitive to the nose radius, a recess is molded into the model to accept the actuator and produce a smooth, flush surface with the airfoil shape. The two copper foil electrodes are aligned in the spanwise direction. They are positioned so that the junction between the exposed and covered electrodes are precisely at the leading edge ($x/c = 0$).

An example of leading-edge separation control on a NACA 0015 airfoil is shown in Fig. 10. This shows the lift coefficient versus angle of attack for the airfoil with the leading-edge plasma actuator off and on in "steady" operation. The measurements are shown as the symbols. The lift forces were measured by a force balance [5]. The curves correspond to numerical flow simulations using a modified version of CFL3D [15] that incorporated the actuator body force effect.

With the actuator off (square symbols), the lift increases linearly up to the stall angle, which is approximately $\alpha = 14$ deg. The solid curve is the numerical prediction without the actuator. Stall corresponds to full leading-edge separation, with a separation bubble that covers the total suction surface of the airfoil. This is documented in the top photograph in the right part of Fig. 10, which shows smoke streaklines over the airfoil at a poststall $\alpha = 16$ deg.

When the actuator is on in steady operation, the stall angle increases to 18 deg. This agrees well with the numerical flow simulation (dashed curve) from Voikov et al. [15] The numerical simulation involves computing the body force distribution based on Eq. (23) for the electrode arrangement used in the experiment. The body force distribution is added to the momentum equation, which, in this case, is solved using CFL3D [15].

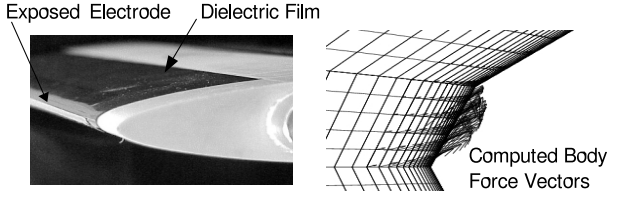

Fig. 9 Photograph of NACA 0015 airfoil model with the plasma actuator applied onto the surface of the airfoil at the leading edge (left) and the computed body force vectors produced by actuator (right).

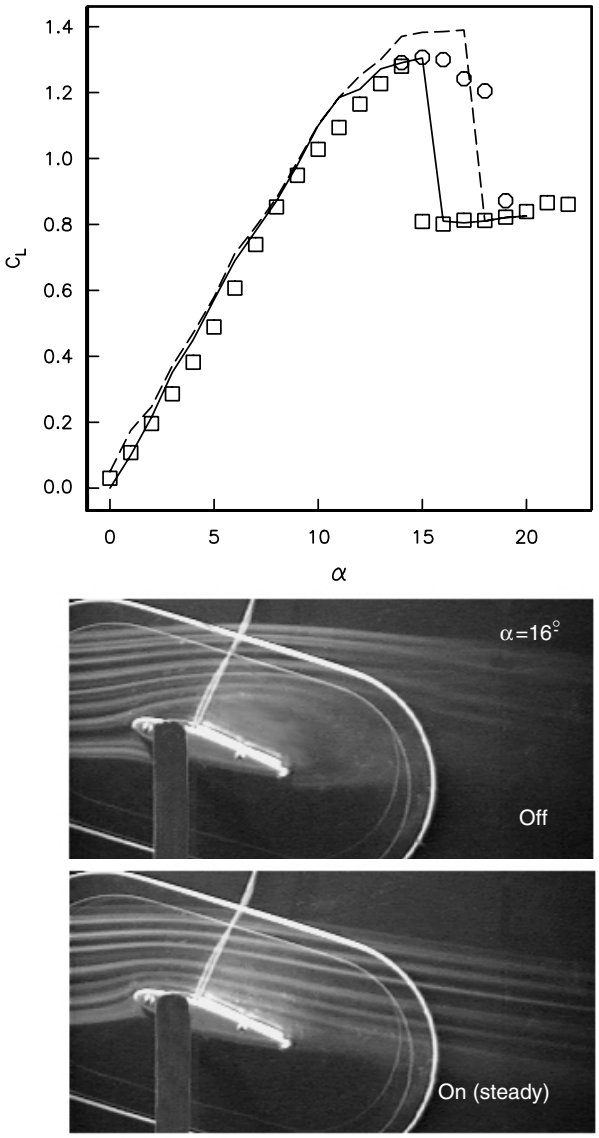

Fig. 10 Lift coefficient versus angle of attack for NACA 0015 airfoil with leading-edge actuator off and on (steady) from Corke et al. [5], and corresponding visualized flow at $\alpha = 16$ deg; from Post [3]. Curves are from numerical simulations by Voikov et al. [15] $U_\infty = 21$ m/s, $Re_c = 0.217 \times 10^6$.

It has been shown in the literature that the introduction of periodic disturbances near the separation location can prevent or delay the onset of separation [29]. The optimum forcing frequency is generally found to occur at a Strouhal number $St = fL_{\text{sep}}/U_\infty \simeq 1$ where L_{sep} is the streamwise extent of the separation zone. For leading-edge separation exhibited here, $L_{\text{sep}} = c$. This has been verified [5] for the experimental conditions in Fig. 10. The result of the optimum unsteady forcing is shown in Fig. 11.

The frequency corresponding to $St = 1$ in this case was an order of magnitude smaller than the frequency of the ac voltage supplied to the actuator. To introduce the lower frequency component, the higher frequency ac voltage is switched on and off at the lower frequency. In addition, the duty time was controllable. An illustration of this is shown in the left part of Fig. 11.

The unsteady actuator with periodic forcing at $St = 1$ gave significantly better results than the steady operation. It substantially increased $C_{L_{\max}}$ and α_{stall}, and maintained lift to $\alpha = 22$ deg, which was 7 deg past the natural stall angle of attack. Similar improvements were also found for higher freestream speeds. These results were obtained while using a 10% duty of the unsteady cycle. As a result, the power to the actuator was only 10% of that for the steady

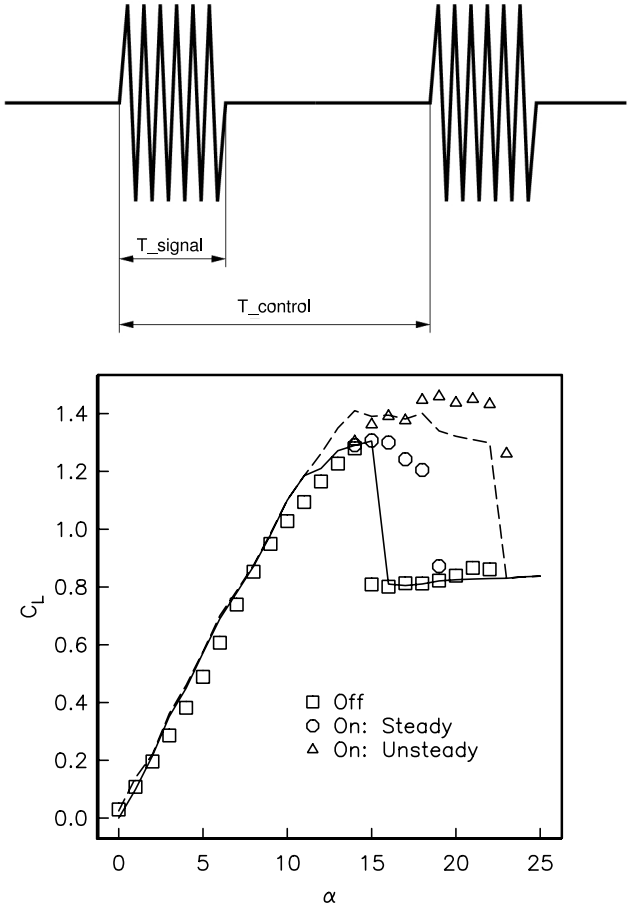

Fig. 11 Lift coefficient versus angle of attack with leading-edge actuator off and on at optimum unsteady Strouhal number, from Corke et al. [5]. Curves are from numerical simulations by Voikov et al. [15]. $U_\infty = 21$ m/s, $Re_c = 0.217 \times 10^6$. Example of time series used as input to actuator for unsteady operation shown at the top.

operation. The power in these cases was approximately 2 W for the 30 cm span.

The results in Fig. 11 with $St = 1$ forcing were again found to agree well with the numerical simulation of Voikov et al. [15]. The simulation again involved adding the body force distribution from the actuator into the momentum equation. The simulation is time dependent, and the effect of the periodic actuation was included by turning the body force on and off at a specified interval in the computational time steps that corresponded to the optimum Strouhal number used in the experiment.

B. Control of Dynamic Stall on Oscillating Airfoils

Plasma actuators for leading-edge separation control of the dynamic stall vortex on an oscillating NACA 0015 airfoil were investigated for the application of control of retreating blade stall on a helicopter rotor. The effectiveness was based on a combination of flow visualization records and pressure measurements on the surface of the airfoil. The results presented here correspond to an angle of attack cycle given by $\alpha(t) = 15\ \text{deg} + 10\ \text{deg} \sin \omega t$, with a reduced frequency of $k = 0.08$. The overall effects of the mean angle of attack, oscillating amplitude, and reduced frequency were investigated by Post [3].

The airfoil was instrumented with an array of surface pressure ports that were used to determine the static pressure distribution, and integrated to obtain the lift during the pitching cycle.

The airfoil was oscillated about its quarter chord location. The motion was driven by a programmable servo motor. Two output encoder signals provided feedback on the instantaneous angle of attack during the pitching cycle.

The plasma actuator configuration used in these experiments was identical to that used in the fixed angle of attack studies presented in the previous section. The actuator spanned most of the width of the airfoil with the exception of a narrow gap at the spanwise centerline, where the pressure taps were located. The actuators were operated either in steady or "unsteady" modes, with the latter being at different unsteady frequencies.

Figure 12 summarizes the flowfield over the suction surface of the oscillating airfoil during the part of the pitch-up portion of the cycle

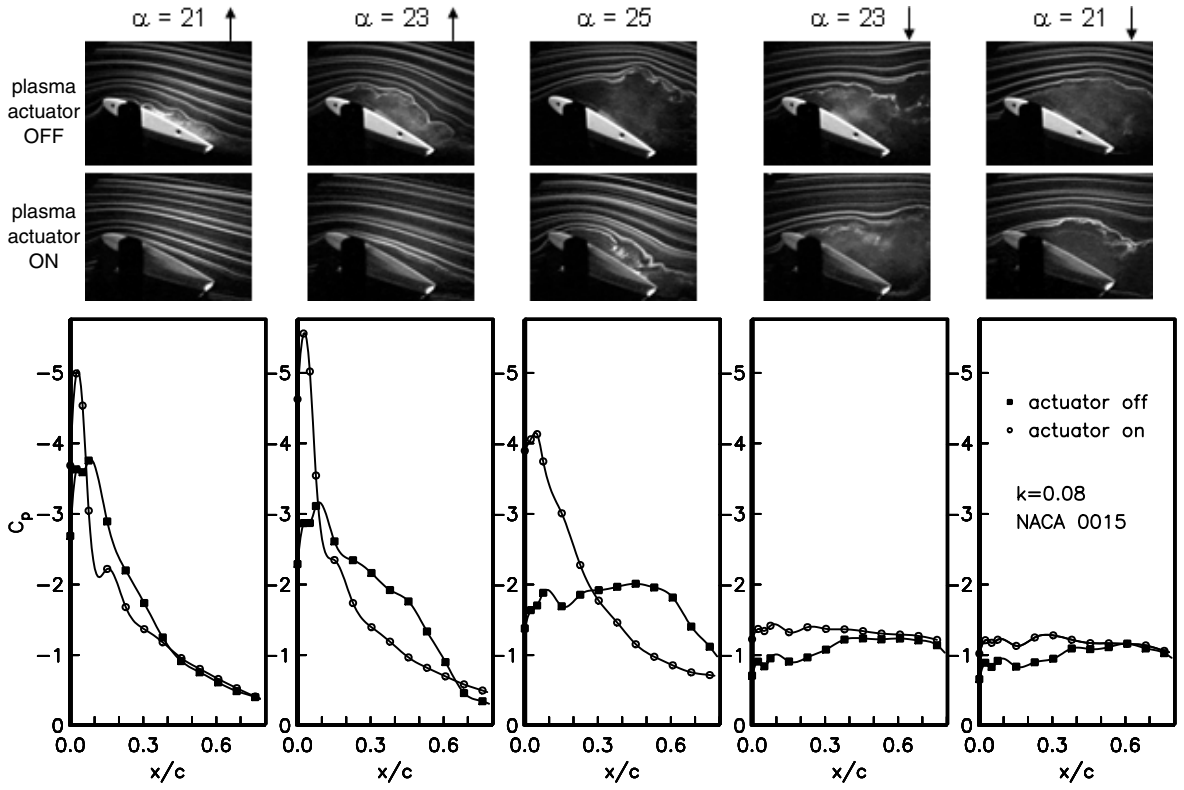

Fig. 12 Flow visualization and pressure coefficient distributions for angles of attack approaching and at the peak in the oscillating airfoil cycle. The instantaneous angle of attack is indicated at the top of the flow visualization images. The arrows indicate if the airfoil is pitching up (↑) or down (↓).

approaching the maximum angle of attack for the cases with the actuator off and on with steady operation. With the actuator off, the dynamic-stall vortex forms at the leading edge and then convects over the upper surface. Its position can be tracked by the location of the "bulge" in the $-C_p$ distribution at the different angles of attack.

The steady actuator is able to suppress the dynamic-stall vortex and maintain a larger $-C_p$ peak at the leading edge up to the maximum angle of attack $\alpha = 25$ deg. At the maximum angle of attack, the complete lack of the pressure bulge is very evident. The flow visualization reveals that a small separation bubble exists with the actuator on, compared with the large separation without the actuator. As a result, the pressure peak is still quite strong at the leading edge and still even exceeds the maximum $-C_p$ value with the actuator off.

The flow eventually separates as the airfoil pitches down, but the flow visualization indicates that it is not separated as much compared with when the actuator was off. As a result, the $-C_p$ distributions are more uniform over the airfoil, with higher (more negative) values within the first one-third chord.

The coefficients of lift for the oscillatory cycle were determined by integrating the pressure distribution around the airfoil for the different discrete angles. The total lift cycle for the conditions in Fig. 12 are presented in the left part of Fig. 13.

The lift coefficient cycle for the case with the actuator off has the characteristic shape observed by others [30]. For the pitch-up portion of the cycle, an almost linear increase in the lift exists with increasing angle of attack, up to approximately $\alpha = 22$ deg. Above this angle, there was a sharp increase in the lift coefficient, which, based on Fig. 12, corresponds to the formation of the dynamic-stall vortex. The initial part of the pitch-down portion of the cycle shows the remnant of the vortex that produces the sharp drop in the lift past $\alpha_{\max}$ and the "lobe" in the initial downstroke portion of the lift cycle that persists to approximately $\alpha = 22$ deg.

With the actuator on, an improvement over most of the cycle is evident. In particular, during the pitch-up motion of the cycle, there is a higher lift coefficient at all angles below $\alpha = 20$ deg. Because the plasma actuator has suppressed the dynamic-stall vortex (evident in the flow visualization records in Fig. 12), the added lift associated with the vortex is also suppressed. This is evident from the elimination of the sharp increase in lift previously seen at $\alpha = 22$ deg, and the loss of the lobe in the lift cycle in the initial pitch-down portion. However, past the initial pitch-down part of the cycle, the plasma actuator results in higher lift.

In the previous section on separation control on the fixed angle of attack airfoil, periodic excitation at $St = fc/U_\infty = 1$ was most effective. Based on this, an actuator frequency of 80 Hz was used to control the dynamic-stall vortex. As before, a 10% duty was used. The result of this is shown in terms of the lift cycle in the right part of Fig. 13. Again, the lift cycle with the actuator off is shown for comparison. Contrasting the two, as well as that for the steady actuator case, the $St = 1$ forcing increased the lift at the lower angles of attack in the pitch-down portion of the cycle. However, at the beginning of the pitch-down phase, the lift is somewhat lower. In addition, the unsteady actuation at 80 Hz left the undesirable rapid C_l drop past $\alpha_{\max}$.

In contrast to the 80 Hz ($St = 1$) excitation, $St = 0.25$ (20 Hz) was examined. Note that 20 Hz is still five times the physical oscillatory

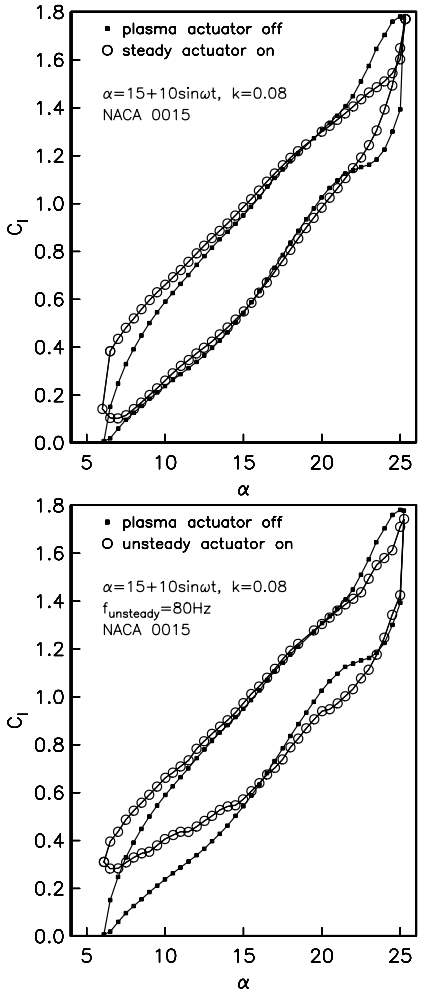

Fig. 13 Comparison of coefficient of lift versus angle of attack with the plasma actuator off and on for the case of steady actuation (top), and for the case of 80 Hz unsteady plasma actuation (bottom). $\alpha = 15 + 10\,\text{deg}\sin\omega t$ and $k = 0.08$.

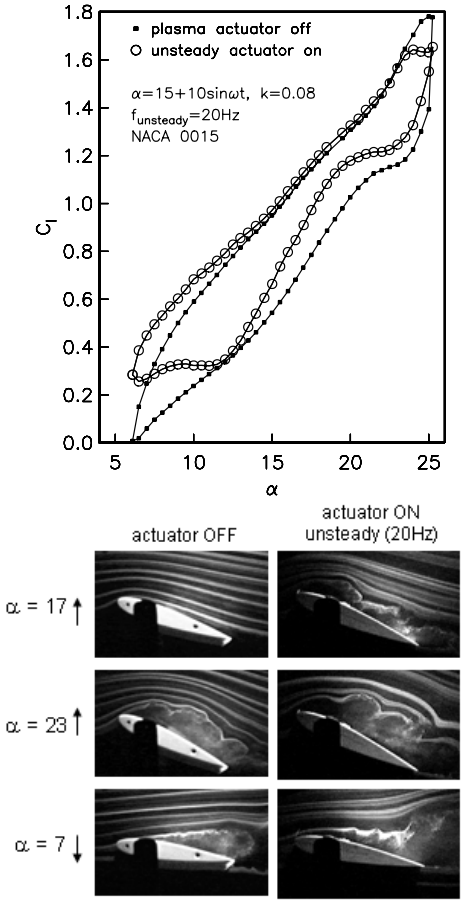

Fig. 14 Comparison of coefficient of lift versus angle of attack with the plasma actuator off and on for the case of 20 Hz unsteady actuation, and corresponding flow visualization records at selected angles. $\alpha = 15 + 10\,\text{deg}\sin\omega t$ and $k = 0.08$. The arrows indicate if the airfoil is pitching up (↑) or down (↓).

frequency of the airfoil (4 Hz). The result of this is shown in terms of the lift cycle and corresponding flow visualization in Fig. 14.

The rationale for the 20 Hz excitation is that this frequency would excite approximately two vortices for each half-cycle of the pitching motion. Having two vortices within the separation zone is the original basis for $St = 1$ that was successful with the stationary airfoil.

The flow visualization photographs for the 20 Hz excitation are contrasted with the equivalent actuator off condition at selected instantaneous angles of attack. At $\alpha = 17$ deg during pitch up, two vortical structures resulting from the actuator are clearly evident. At $\alpha = 23$ deg during pitch up, two to three structures are evident. Three structures are visible during pitch down at $\alpha = 7$ deg. Such flow visualization records confirm the effectiveness of the unsteady actuation on the flowfield.

The $St = 0.25$ excitation results in a significant improvement of the lift cycle compared with the other control cases. In particular, there is a higher lift over the entire pitch-down portion of the cycle, most noticeably in the range from $25 \geq \alpha \geq 13$ deg; a higher lift at the bottom of the pitch-down phase, that persists for the first half of the pitch-up phase; and a more gradual dynamic stall.

The improvements in the cycle-integrated lift resulting from the actuation are summarized in Table 1. These clearly illustrate the greater effectiveness of periodic excitation and the sensitivity to the excitation frequency. With the proper choice (20 Hz in this case), the lift improvement was 10%. These are examples of open-loop control. Further improvement is possible with feedback control. One approach used by Post and Corke [3,4] obtained an overall lift improvement of 12.6%.

C. Control of Separation for Low-Pressure Turbine Stage of Gas-Turbine Engines

This work involves the control of flow separation that occurs over turbine blades in the low-pressure turbine (LPT) stage of gas turbine engines at low blade-chord Reynolds numbers typical of high altitude cruise. This uses a specially constructed linear cascade to study the flow field through a generic LPT cascade made up of Pratt & Whitney "Pak-B" shaped blades. The center blade in the cascade was instrumented to measure the surface pressure distribution. laser Doppler velocimetry (LDV) measurements were also made to obtain boundary layer profiles over the center blade. Details of the facility and results are given by Huang et al. [2,20] and Huang [21]. Representative results are presented here.

Figure 15 shows a photograph of one of the Pak-B blades that make up the cascade of nine blades. The blades were cast in an acrylic polymer from a numerically machined aluminum mold. The chord dimension was 20.05 cm, and the span dimension was 0.84 m. It was molded with 40 pressure ports on the surface. A majority of the taps were on the suction side of the blade, with a greater concentration in the region of $0.5 \leq x/C \leq 0.7$, where the flow separates at lower Reynolds numbers. The pressure taps were located at the half-span position of the blade and were distributed in the chordwise direction. The instrumented blade was the center blade of the nine-blade cascade.

Mean velocity profiles over the blade and surface pressure measurements were used to define the region of flow separation and reattachment (when it occurred) for a range of conditions such as chord Reynolds number and freestream turbulence level. An example of the mean velocity profiles and surface pressure distributions is shown in Fig. 16. The experiments [2] indicated that the location of the flow separation was insensitive to the different

Table 1 Cycle-integrated lift improvement with leading-edge plasma actuator

Actuator condition	% improvement
80 Hz excitation	4.7
Steady excitation	5.4
20 Hz excitation	10.1
Steady closed loop	12.6

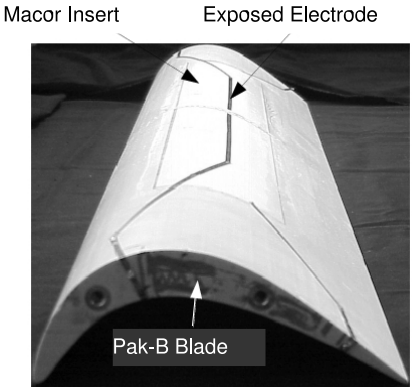

Fig. 15 Photograph of Pak-B blade with single actuator exposed electrode at the 67% chord location on the suction side of the blade. Dielectric for plasma actuator is Macor, which is inset in the blade. Pressure taps are at midspan. From Huang et al. [2,20,21]

conditions. This was important because it allowed the placement of the plasma actuator at a single, fixed location on the blade. This location was at $x/C = 0.67$, which was just upstream of the flow separation line.

The design of the plasma actuator used to control the flow separation on the blade was similar to that shown in Fig. 1. The exposed electrode in this case can be seen in the photograph in Fig. 15. The dielectric material used was Macor (a machinable ceramic), which was shaped to match the blade profile. The actuator spans most of the blade. A gap is left at the center span at the location of the pressure taps.

The plasma actuator was designed to induce flow toward and along the blade surface in the downstream direction to add momentum to the separated flow and cause it to reattach. Both steady and unsteady operation of the actuator were investigated.

Figure 16 shows results at an intermediate chord Reynolds number of 50 K. The left part of the figure shows mean velocity profiles with the actuator off (open symbols) and on (closed symbols) in unsteady operation with $St \simeq 1$. The mean velocity profiles with the actuator off indicate a large separation bubble that extends from $x/c = 0.7$ to 0.95. The pressure distributions in the right part of Fig. 16 are used to further define the separation and reattachment locations and the effect of the plasma actuator. The solid curve corresponds to the inviscid (infinite Reynolds number) C_p distribution. At large enough Reynolds numbers at which the flow remains attached, the agreement between the experiment and inviscid calculation were excellent [2,21]. Therefore, any deviation from the inviscid distribution was an indication of flow separation.

For the case with the actuator off (circles), the $-C_p$ distribution begins to deviate from the inviscid distribution at $x/C = 0.6$; however, the separation location is determined to be where the pressure distribution forms a plateau, which in this case starts at $x/C \simeq 0.72$. The reattachment location is defined to be where the C_p values return to the inviscid curve. With the actuator off, this was at $x/C \simeq 0.95$.

The effect of the steady plasma actuator is shown as the triangle symbols. This shows a smaller plateau in the C_p distribution indicating a small separation bubble remaining with reattachment at $x/C \simeq 0.85$.

The effect of the unsteady ($St \simeq 1$) actuator is to completely remove the plateau in the C_p distribution. This indicates that the flow remains attached. Measurements at different actuator frequencies showed a clear optimum at $St \simeq 1$ [20,21].

To understand the mechanism behind the unsteady plasma actuators, we again started with flow visualization. A sample of these is shown in Fig. 17. This shows three consecutive frames from a video in which the unsteady actuator was operating at 20 Hz and the laser light sheet used to illuminate the visualization particles was chopped at 21 Hz to produce a difference frequency of 1 Hz.

The principle behind the use of the unsteady plasma actuator was to generate spanwise vortices that could bring high momentum fluid

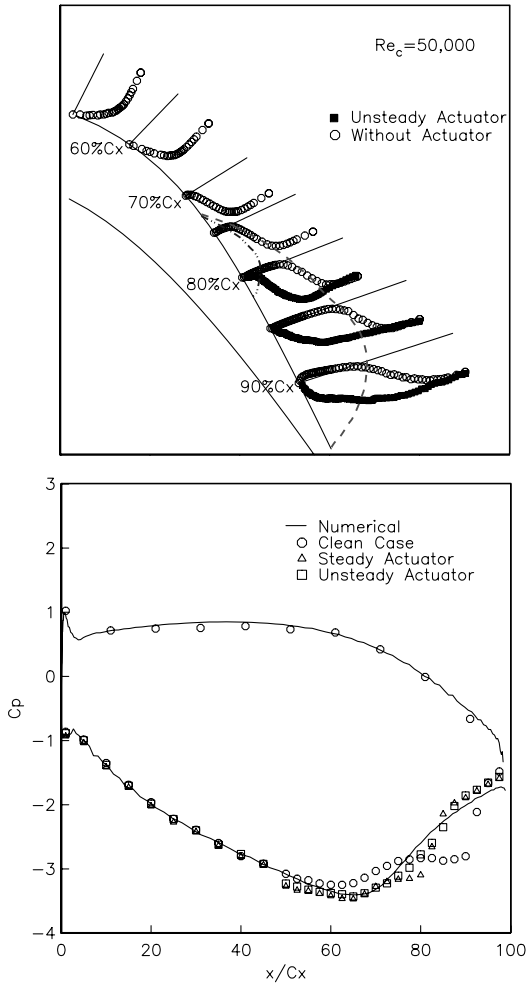

Fig. 16 The boundary layer profiles on Pak-B blade with a unsteady actuator operating and not operating at $Re_c = 50 \times 10^4$. The single plasma actuator was located at $x/C_x = 67.5\%$, operated at 100 Hz ($S_t = 0.9$), and the duty cycle was 10%. The boundary of the separation bubbles are sketched using dashed lines. From Huang et al. [20,21].

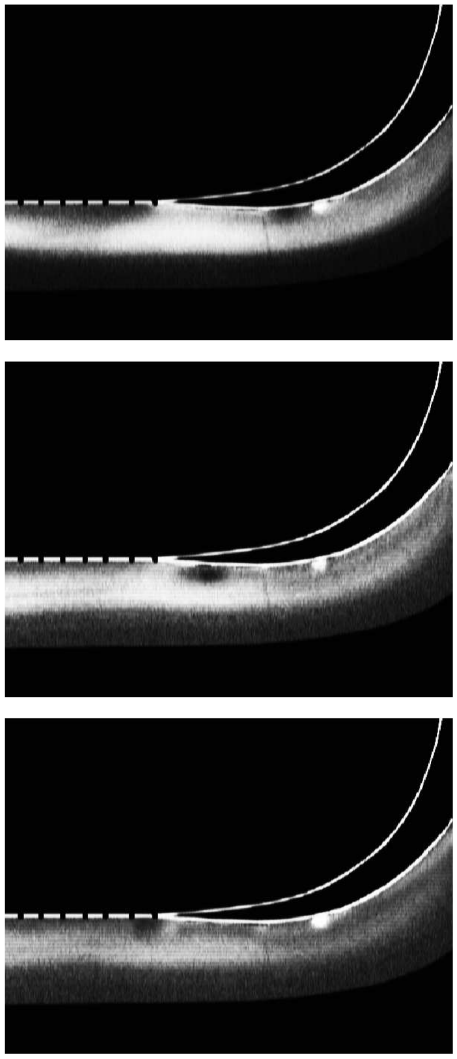

Fig. 17 Three consecutive frames taken from video records for $Re_c = 2.5 \times 10^4$ showing the visualized flow over the suction side of a blade in a linear cascade that documents the flow structure produced by an unsteady plasma actuator on the blade surface. From Huang et al. [20].

towards the blade surface. Although the flow visualization cannot provide quantitative evidence of spanwise vortices, we can observe periodic features that are being convected downstream of the actuator. These appear as dark regions over the surface of the blade. The top image in Fig. 17 shows this dark feature just downstream of the actuator on the blade surface. The middle image is 1/30 s later. This shows the dark feature moved to a location near the trailing edge of the blade. In the last image in the sequence, the dark feature is off the end of the blade. Accounting for the time difference between images, the convection speed can be estimated to be

$$U_c = \frac{\Delta x}{\Delta t} = 2.33 \text{ (m/s)} \tag{24}$$

The local freestream velocity at blade Reynolds number (2.5×10^4) for these images was 4.7 m/s. Therefore, the convection velocity of these features was approximately half of the midchannel velocity ($0.5U_{\text{midchannel}}$), which is the expected convection speed for spanwise vortices. The same mechanism is expected for the unsteady separation control applications demonstrated in the previous sections.

IV. Conclusions

The SDBD plasma actuators have proven to be effective in controlling flow separations in a variety of flow applications. When placed at the leading edge of wing sections at large angles of attack well past stall, as much as a 400% increase in the lift-to-drag ratio has been consistently obtained. Similar leading-edge actuator designs were effective in controlling the dynamic-stall vortex on oscillating airfoils simulating helicopter rotors. In this application, as much as a 13% improvement in the cycle-integrated lift was obtained. The actuators were also effective at completely suppressing separation that occurs near the midchord region of blades in a linear cascade simulating the conditions in the LPT stage of gas-turbine engines. In all cases, periodic excitation of the actuator with a short duty cycle was more effective than steady actuation. The optimum excitation frequency was generally one that could produce approximately two spanwise vortices in the streamwise length of the separation zone.

In addition to the experimental use of the plasma actuators, models for the space–time evolution of the plasma generation over the actuator and a first-principle formulation for the body force produced by the plasma on the ambient flow have been implemented in numerical flow solvers. These have produced excellent agreement with experiments on leading-edge separation control in both steady and unsteady cases. Their purpose is to provide simulations that can be used in optimizing the design and placement of plasma actuators for different applications of flow control to enhance aerodynamic performance.

Acknowledgments

The work presented in this paper has resulted from the support of a number of grants and contracts. These include a grant from Defense

Advanced Research Projects Agency/Army Research Office number DAAD19-00-1-0447, a grant from the NASA Glenn Research Center number NCC3-775, and Small Business Innovative Research Phases I and II with Orbital Research, Inc., supported by the United States Air Force/Air Force Research Lab Wright Patterson Air Force Base under contract numbers F33615-03-M-3327 and FA8650-04-C-3405, monitored by Charles Suchomel. Mehul Patel is the Principle Investigator/Program Manager at Orbital Research, Inc.

References

[1] Post, M., and Corke, T., "Separation Control on High Angle of Attack Airfoil Using Plasma Actuators," AIAA Paper 2003-1024, 2003; also *AIAA Journal*, Vol. 42, No. 11, 2004, pp. 2177. doi:10.2514/1.2929

[2] Huang, J., Corke, T., and Thomas, F., "Plasma Actuators for Separation Control of Low Pressure Turbine Blades," AIAA Paper 2003-1027, 2003; also *AIAA Journal*, Vol. 44, No. 1, pp. 51–58. doi:10.2514/1.2903

[3] Post, M., "Plasma Actuators for Separation Control on Stationary and Oscillating Wings," Ph.D. Dissertation, University of Notre Dame, Notre Dame, IN, 2004.

[4] Post, M., and Corke, T., "Separation Control Using Plasma Actuators: Stationary and Oscillating Airfoils," AIAA Paper 2004-0841, 2004.

[5] Corke, T., He, C., and Patel, M., "Plasma Flaps and Slats: An Application of Weakly-Ionized Plasma Actuators," AIAA Paper 2004-2127, 2004.

[6] Corke, T., Jumper, E., Post, M., Orlov, D., and McLaughlin, T., "Application of Weakly-Ionized Plasmas as Wing Flow-Control Devices," AIAA Paper 2002-0350, 2002.

[7] Corke, T., Mertz, B., and Patel, M., "Plasma Flow Control Optimized Airfoil," AIAA Paper 2006-1208, 2006.

[8] Enloe, L., McLaughlin, T., VanDyken, R. D., Kachner, K. D., Jumper, E., and Corke, T., "Mechanisms and Response of a Single Dielectric Barrier Plasma Actuator: Plasma Morphology," *AIAA Journal*, Vol. 42, No. 3, 2004, p. 589; also AIAA Paper 2003-1021, 2003.

[9] Enloe, L., McLaughlin, T., VanDyken, R. D., Kachner, K. D., Jumper, E., Corke, T., Post, M., and Haddad, O., "Mechanisms and Response of a Single Dielectric Barrier Plasma Actuator: Geometric Effects," *AIAA Journal*, Vol. 42, No. 3, 2004, p 585.

[10] Massines, F., Rabehi, A., Decomps, P., BenGadri, R., Segur, P., and Mayoux, C., "Experimental and Theoretical Study of a Glow Discharge at Atmospheric Pressure Controlled by Dielectric Barrier," *Journal of Applied Physics*, Vol. 83, No. 6, 1998, p. 2950. doi:10.1063/1.367051

[11] Paulus, M., Stals, L., Rude, U., and Rauschenbach, B., "Two-Dimensional Simulation of Plasma-Based Ion Implantation," *Journal of Applied Physics*, Vol. 85, No. 2, 1999, p. 761. doi:10.1063/1.369157

[12] Orlov, D., Corke, T., and Patel, M., "Electric Circuit Model for Aerodynamic Plasma Actuator," AIAA Paper 2006-1206, 2006.

[13] Orlov, D., Corke, T., and Haddad, O., "DNS Modeling of Plasma Actuators," *Bulletin of the American Physical Society, Program of the 56th Meeting of the Division of Fluid Dynamics*, Vol. 48, No. 10, Nov. 2003, JA004.

[14] Orlov, D., and Corke, T., "Numerical Simulation of Aerodynamic Plasma Actuator Effects," AIAA Paper 2005-1083, 2005.

[15] Voikov, V., Corke, T., and Haddad, O., "Numerical Simulation of Flow Control over Airfoils Using Plasma Actuators," *Bulletin of the American Physical Society, Program of the 57th Annual Meeting of the Division of Fluid Dynamics*, Vol. 49, No. 9, Nov. 2004, FG008.

[16] Roth, J. R., "Industrial Plasma Engineering," Vol 1, Inst. of Physics Publishing, London, 1995, p. 538.

[17] Orlov, D., Corke, T., and Post, M., "DNS Modeling of Plasma Array Flow Actuators," *Bulletin of the American Physical Society, Program of the 55th Annual Meeting of the Division of Fluid Dynamics*, Vol. 47, No. 10, Nov. 2002, EG009.

[18] Orlov, D., Corke, T., and Haddad, O., "Modeling of Plasma Actuator Effects Using Lumped Element Circuit Model," *Bulletin of the American Physical Society, Program of the 57th Annual Meeting of the Division of Fluid Dynamics*, Vol. 49, No. 9, Nov. 2004, FG009.

[19] Corke, T., Cavalieri, D., and Matlis, E., "Boundary Layer Instability on a Sharp Cone at Mach 3.5 with Controlled Input," *AIAA Journal*, Vol. 40, No. 5, 2001, pp. 1015–1017.

[20] Huang, J., Corke, T., and Thomas, F., "Unsteady Plasma Actuators for Separation Control of Low Pressure Turbine Blades," *AIAA Journal*, Vol. 44, No. 7, 2006, pp. 1477–1487. doi:10.2514/1.19243

[21] Huang, J., "Documentation and Control of Flow Separation on a Linear Cascade of Pak-B Blades Using Plasma Actuators," Ph.D. Dissertation, University of Notre Dame, Notre Dame, IN, 2005.

[22] Hultgren, L., and Ashpis, D., "Demonstration Of Separation Delay With Glow-Discharge Plasma Actuators," AIAA Paper 2003-1025, 2003.

[23] Balcer, B., Franke, M., and Rivir, R., "Effects Of Plasma Induced Velocity On Boundary Layer Flow," AIAA Paper 2006-0875, 2006.

[24] Visbal, M., and Gaitonde, D., "Control Of Vortical Flows Using Simulated Plasma Actuators," AIAA Paper 2006-0505, 2006.

[25] Wilkinson, S., "Investigation of an Oscillating Surface Plasma for Turbulent Drag Reduction," AIAA Paper 2003-1023, 2003.

[26] Gaitonde, D., Visbal, M., and Roy, S., "Modeling Surface Discharge Effects of Atmospheric RF on Gas Flow Control," AIAA Paper 2005-0160, 2005.

[27] Suzen, Y., and Huang, P., Jacob, J., and Ashpis, D., "Numerical Simulations of Plasma Based Flow Control Applications," AIAA Paper 2005-4633, 2006.

[28] Suzen, Y., and Huang, P., "Simulation of Flow Separation Control Using Plasma Actuators," AIAA Paper 2006-0877, 2006.

[29] Seifert, A., Bachar, T., Moss, D., Shepshelovish, M., and Wygnanski, I., "Oscillatory Blowing: A Tool to Delay Boundary-Layer Separation," *AIAA Journal*, Vol. 11, No. 31, 1993, pp. 2052–2060.

[30] Leishman, J., Gordon., *Principles of Helicopter Aerodynamics*, Cambridge Univ. Press, New York, 2000.

[31] Orlov, D., "Modeling and Simulation of Single Dielectric Barrier Discharge Plasma Actuators,".Ph.D. Dissertation, University of Notre Dame, Notre Dame, IN, 2006.

S. Macheret
Guest Editor